LIQT: Bridging Liquid Neural Dynamics and Human Perceptual Mechanisms for Blind Image Quality Assessment

Anonymous authors

000

001

002

004

006

012 013

014

016

018

019

020

021

022

024

025

026

027

028

031

033

034

037

038

040 041

042

043

044

046

047

048

051

052

Paper under double-blind review

ABSTRACT

Blind Image Quality Assessment (BIQA) seeks to predict perceptual quality in reference-free scenarios, yet conventional methods often hard to capture the human visual system's adaptive spatio-temporal integration of degradation pat-Inspired by the adaptive temporal dynamics of biological neural circuits, we propose Liquid Image Quality Transformer (LIQT), a novel BIQA framework that integrates Liquid Neural Networks (LNNs) with Transformerbased architectures. LIQT incorporates Liquid Self-Attention (LSA) equipped with Closed-Form Continuous-Time Module (CFCTM), which reformulates liquid time-constant neurons into stable closed-form solutions through learnable decay rates and Padé approximation, thus enabling LIQT to dynamically modulates feature extraction based on local image features. To emulate multi-scale perceptual evaluation, a Multi-Scale Image Quality-Aware Decoder (MIQAD) aggregates multi-scale features from LIOT for comprehensive quality regression. This work pioneers the integration of biomimetic neural mechanisms into BIQA and experiments in six benchmark datasets that span various types of distortion and image content demonstrate the superior performance of LIQT over state-of-theart methods.

1 Introduction

Image quality assessment (IQA) aims to evaluate perceptual quality in alignment with human judgment, serving as a critical tool for optimizing image processing algorithms and benchmarking visual content fidelity Wang et al. (2004). Based on the availability of the pristine reference image, IQA can be typically divided into full-reference IQA (FR-IQA), reduced-reference IQA (RR-IQA), and no-reference or blind IQA (BIQA) Moorthy & Bovik (2011). FR-IQA and RR-IQA rely on complete or partial reference images, limiting their applicability in real-world scenarios where pristine references are typically absent. BIQA has garnered increasing attention by addressing this limitation through its reference-free operation, yet it remains inherently challenged in modeling the nonlinear relationship between distortions and human perception Yang et al. (2019).

BIQA task exhibits unique characteristics distinct from conventional visual tasks, particularly in its manifestation of disjoint processing of spatio-temporally continuous degradation information, where temporal memory updating and spatial feature extraction operate in decoupled optimization spaces Zhang et al. (2023), we refer this challenge as "Spatio-Temporal Representation Disentanglement (STRD)". The human visual system (HVS) accomplishes quality evaluation through continuous-time neural dynamics van den Branden Lambrecht (1996), as illustrated in Figure 1(a), the HVS integrates historical perceptual experiences via spatio-temporal memory consolidation mechanisms to generate adaptive assessments for varying degradation images of the same type of object. This adaptive capability is driven by HVS's neural sensitivity to spatial contextual correlations and temporal persistence representations Yan et al. (2020). However, current CNN-based or Transformer-based BIQA methods hard to establish continuous memory mapping across distortion types and degradation levels for BIQA tasks because of this STRD challenge.

Liquid Neural Networks (LNNs) implement a biomimetic framework inspired by the neurophysiological mechanisms of *Caenorhabditis elegans* Hasani et al. (2020), employing Liquid Time-

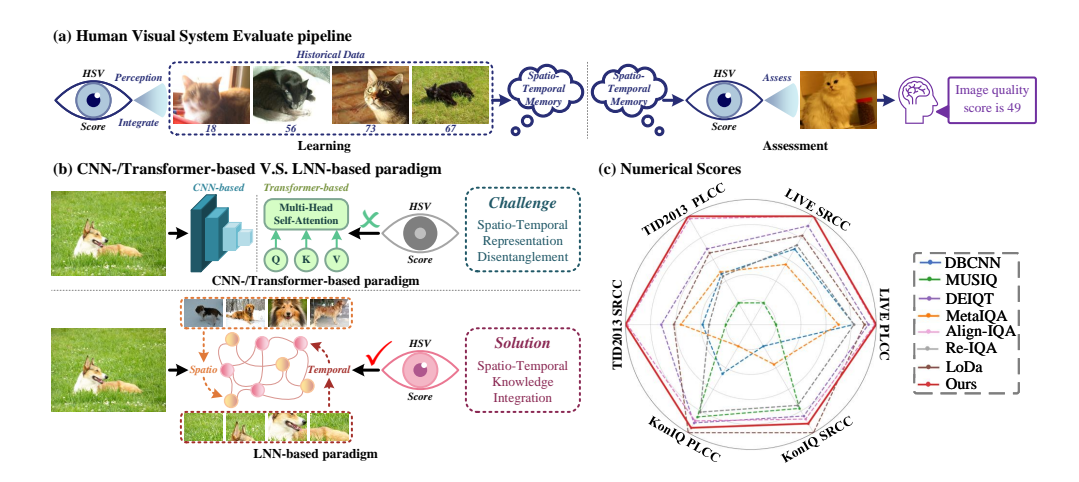


Figure 1: (a) Human Visual System Evaluate pipeline, the HVS integrates historical perceptual experiences via spatio-temporal memory consolidation mechanisms to generate adaptive assessments for varying degradation images of the same type of object. (b) The CNN-/Transformer-based paradigm suffer from STRD challenge, hard to establish continuous memory mapping across distortion types and degradation levels for BIQA tasks. LNN-based paradigm address the STRD challenge through Spatio-Temporal Knowledge Integration. (c) Comparison of seven state-of-the-art methods and LIQT performance based on the average values of PLCC and SRCC across three benchmark datasets.

Constant (LTC) neurons with input-dependent synaptic gating to dynamically modulate temporal dynamics through closed-form solutions Hasani et al. (2022). This approach has demonstrated efficacy in sequential decision-making and adaptive control tasks by emulating biological neural circuit behaviors Lechner et al. (2020); Chahine et al. (2023). Despite their demonstrated efficacy, LNNs exhibit a limitation in that they primarily focus on temporal dynamics and sequential processing, thus constraining their ability to effectively extract and interpret complex deep features and spatial contextual information within individual images.

To this end, we propose a novel BIQA method, Liquid Image Quality Transformer (LIQT), a framework that embeds LNNs into a Transformer-based architecture. Specifically, the Closed-Form Continuous-Time Module (CFCTM) reformulates liquid neuronal dynamics into stable closed-form solutions, replacing iterative differential equation solving with learnable decay rates and Padé approximations. CFCTM integrates into the Liquid Time-Constant Transformer (LTCFormer), each LTCFormer block uses Liquid Self-Attention (LSA) to combine CFCTM with self-attention, enabling adaptive feature processing based on local image features. Finally, a Multi-Scale Image Quality-Aware Decoder (MIQAD) aggregates features across hierarchical stages to emulate the simultaneous evaluation of fine details and global composition by human observers. Our LIQT model is designed with computational efficiency in mind, achieving strong performance with a significantly reduced parameter count.

In summary, the contributions of this paper are the following:

- We propose the Liquid Image Quality Transformer (LIQT), the first framework to incorporate LNNs into BIQA task, which integrates continuous-time neural dynamics through CFCTM, enabling adaptive temporal processing aligned with human visual mechanisms.
- We propose the Liquid Time-Constant Transformer (LTCFormer), extend the principles of adaptive temporal scaling in sequential tasks to spatial domains.
- Inspired by the LNNs, we introduce a novel closed-form implementation of liquid timeconstant neurons, built on closed-form solutions from continuous-time network research, enabling stable integration with Transformer-based architecture.
- We verify our lightweight LIQT on 6 benchmark IQA datasets involving a wide range of image contents, distortion types, and dataset size. LIQT outperforms other competitors across all these datasets.

2 RELATED WORKS

Liquid Neural Networks. Recent advances in LNNs have demonstrated their potential to model dynamic systems through continuous-time differential equations and closed-form approximations. Hasani et al. (2020) introduced Liquid Time-Constant (LTC) networks, leverage input-dependent synaptic gating inspired by the neurophysiology of *Caenorhabditis elegans*, enabling adaptive temporal dynamics for sequential tasks such as autonomous navigation and prediction of time series. Lechner et al. (2020) demonstrated auditable autonomy in autonomous vehicles using compact, interpretable architectures with only 19 neurons, underscoring LNNs' efficiency and transparency. Hasani et al. (2022) further improved computational efficiency by replacing iterative differential equation solvers with analytical approximations, achieving speed improvements while retaining ro-

bustness and causal reasoning capabilities. Karn et al. (2024) have expanded LNNs applications beyond sequential tasks to non-causal domains, creating a unified mathematical framework that bridges temporal and spatial processing. Ayoub et al. (2024) have explored how the adaptive properties of LNNs can enhance learning in dynamic environments by leveraging input-dependent time constants to mitigate catastrophic forgetting.

Blind Image Quality Assessment. The development of deep learning has advanced the field of image quality assessment (IQA). Early IQA methods depended on handcrafted features for quality evaluation. However, this approach couldn't handle the complexity of blind image quality assessment (BIQA) tasks. Some CNN-based methods have achieved good results in BIQA tasks Saha et al. (2023); Zhao et al. (2023), but still struggle with CNNs' tendency to focus on local features, making it difficult to obtain an overall quality score for the image. Vision Transformers Dosovitskiy et al. (2021) have provided a new solution for BIQA, achieving good results through their excellent global context understanding Chen et al. (2024). Multi-scale feature adaption, cross-attention, or comparison technique have been used to solve the inherent efficiency issues in ViT Qin et al. (2023); Ke et al. (2021). Recently, state space models have emerged as an alternative approach, with QMamba Guan et al. (2025) demonstrating the effectiveness of selective state space mechanisms in capturing long-range dependencies for quality assessment while maintaining computational efficiency.

3 METHODOLOGY

3.1 Overall Architecture

The overall architecture of the proposed Liquid Image Quality Transformer (LIQT) is illustrated in Figure 2, consists of three components: Liquid Time-Constant Transformer (LTCFormer), Closed-Form Continuous-Time Module (CFCTM), and Multi-Scale Image Quality-Aware Decoder (MIQAD). LTCFormer processes input images via window tokenization, splitting images into patch tokens and embedding them into spatiotemporal representations. CFCTM dynamically models temporal responses using LTC neurons, simulating biological visual processing through learnable decay rates and adaptive gating mechanisms. Each LTCFormer block uses Liquid Self-Attention (LSA) to combine CFCTM with self-attention, enabling adaptive feature processing based on local image features. The LTCFormer employs a four-stage architecture to extract multi-scale features, progressively generating representations with different dimensions. These hierarchical feature maps are subsequently processed by the MIQAD module, which conducts multi-scale quality assessment through global average pooling followed by scale-specific quality score prediction using MLP-based regression.

3.2 LIQUID TIME-CONSTANT TRANSFORMER

To maintain efficiency, former Transformer-based networks generally employ static attention mechanisms within small patches Chen et al. (2021); Dosovitskiy et al. (2021) or local windows Liu et al. (2021; 2022), potentially hindering the simulation of adaptive temporal dynamics inherent in visual processing. Motivated by the success of LNNs in continuous-time dynamic modeling Hasani et al. (2020); Lechner et al. (2020), we propose the Liquid Time-Constant Transformer (LTCFormer) to enhance visual models' continuous-time modeling capabilities.

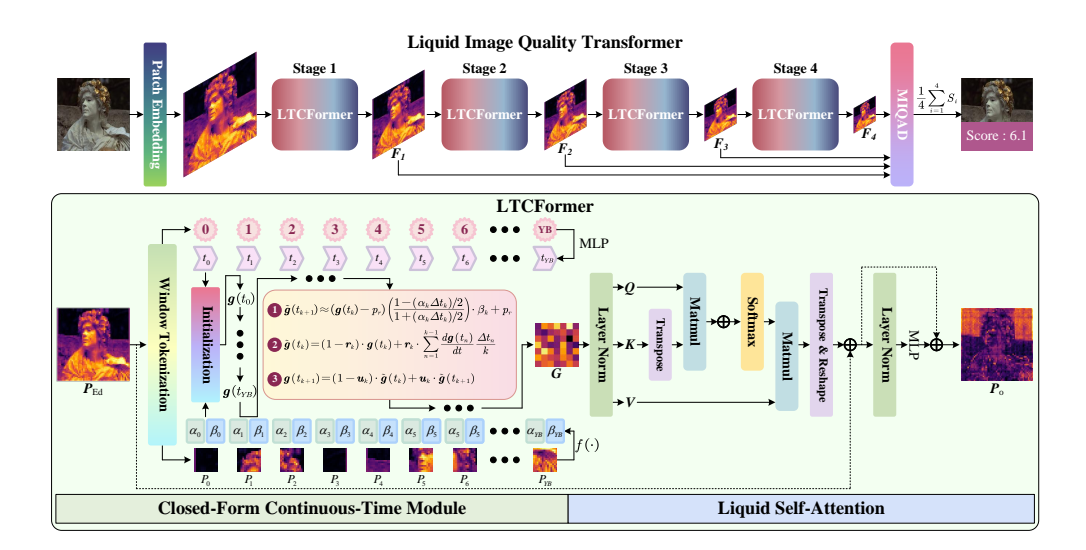


Figure 2: The overall framework of the proposed LIQT.

3.2.1 WINDOW TOKENIZATION

As illustrated in Figure 2, given an input image $I \in \mathbb{R}^{B \times H \times W \times C}$, where B, H, W, and C denote the batch size, height, width, and channel dimensions, respectively. We first perform the patch partition operation with the patch size of d and flatten each patch into a set of patch tokens $P \in \mathbb{R}^{B \times (HW/d^2) \times C}$. The HVS evaluates images through a neural process where both spatial context and temporal memory interact dynamically, rather than treating each region independently Chandler (2010). To model this integrated process in our framework, we transform spatial relationships into a temporal sequence by organizing image patches into windows where position encodes temporal ordering. This approach addresses the STRD challenge by mapping spatial adjacency relationships to sequential processing steps, allowing our model to leverage the continuous-time dynamics of LNNs to simulate how human observers progressively integrate local features with contextual information. Specifically, we partition patches into $Y = (H/dT) \times (W/dT)$ windows of size $T \times T$, where Y refers to the number of windows. A linear embedding layer then projects these patches into a dimensional space L, generating patch embeddings $P_{\rm Ed} \in \mathbb{R}^{YB \times T^2 \times L}$. Subsequently, we perform the window partition operation on $P_{\rm Ed}$ to obtain the partitioned $P_{\rm w} \in \mathbb{R}^{YB \times T^2 \times L}$ and the position embedding $M \in \mathbb{R}^{YB \times T^2 \times T}$ that preserves the relative position of a patch for the windows. The obtained $P_{\rm w}$ and M are then fed into CFCTM to model dynamic temporal responses in continuous time.

3.2.2 Closed-Form Continuous-Time Module

The human visual system (HVS) processes visual stimuli through complex neural interactions that evolve continuously over time, adapting to local image features Chandler (2010). In BIQA tasks, simulating this adaptive mechanism is crucial to improve the effect of quality evaluation. We first define the Liquid Time-Constant (LTC) neurons that form the basis of our approach, the membrane potential $\boldsymbol{g}(t)$ of LTC neurons is determined by the solution of the following initial value problem Hasani et al. (2020):

$$\frac{d\boldsymbol{g}(t)}{dt} = -\left[\boldsymbol{l} + f\left(\boldsymbol{P}(t)\right)\right] \cdot \boldsymbol{g}(t) + f\left(\boldsymbol{P}(t)\right) \cdot p_r,\tag{1}$$

where t represents time, l denotes the leakage conductance vector of the LTC neurons Lechner et al. (2020), P(t) is the exogenous input signal, $f(\cdot)$ represents nonlinear functions of synaptic inputs, and p_T indicates the reversal potential of LTC neurons.

To enhance the applicability of LTC neurons models in vision-related tasks, we reformulate Eq.1 into a computationally stable and learnable representation. By introducing two learnable parameters $\alpha_k = l + f(P_k)$ as the decay rate and $\beta_k = f(P_k)$ as the modulation factor, we can derive an

expression for membrane potential evolution over time intervals:

$$\frac{d\boldsymbol{g}\left(t\right)}{dt} = -\alpha_k \cdot \boldsymbol{g}\left(t\right) + \beta_k \cdot p_r,\tag{2}$$

where α_k controls the rate of the signal attenuates, and β_k modulates the efficiency of inputs transmission efficiency. Thus, the closed-form solution to this differential equation can be formulated as Hasani et al. (2022):

$$\mathbf{g}(t) \approx (\mathbf{g}_0 - p_r) e^{-\alpha_k t} \cdot \beta_k + p_r,$$
 (3)

where g_0 represents the initial membrane potential. Eq.1 and Eq.3 describe the basic behavior of LTC neurons, but present challenges for direct application to vision tasks. To be specific, Eq.2 assumes that the input I(t) remains piecewise constant over specific time intervals Hasani et al. (2022); Ayoub et al. (2024). This property is a reasonable assumption for causal signals that involve a sequential nature but poses challenges when transferring to non-causal data such as images Karn et al. (2024).

This MLP learns a nonlinear mapping that converts spatial distance relationships between patches into temporal intervals, effectively creating a manifold that preserves locality while enabling differential equation dynamics across the image structure. During training, the MLP develops a transformation that prioritizes quality-relevant spatial adjacencies as temporal proximities, allowing our continuous-time framework to process spatial relationships through biologically-inspired neural dynamics.

To address this, we flatten M through a multi-layer perceptron (MLP) layer to transform spatial positions into time parameters, which converts each window's position into a corresponding time step on a temporal axis. This MLP layer learns a nonlinear mapping that converts spatial distance relationships between patches into temporal intervals, creating a manifold that preserves locality while enabling differential equation dynamics across the image structure. During training, the MLP develops a transformation that prioritizes quality-relevant spatial adjacencies as temporal proximities, allowing our continuous-time framework to process spatial relationships through biologically-inspired neural dynamics. Next, partition the time parameters into N sub-intervals, taking k-th time interval $[t_k, t_{k+1}]$ and the corresponding state $g(t_k)$, Eq.2 can be parameterized as:

$$\tilde{\mathbf{g}}(t_{k+1}) \approx (\mathbf{g}(t_k) - p_r) e^{-\alpha_k \Delta t_k} \cdot \beta_k + p_r, \tag{4}$$

where $\Delta t_k = t_{k+1} - t_k$ represents the length of the interval. And to facilitate Eq.4 for stability of the tensor for large-scale image processing, we employ the (1,1)-order Padé approximant to $e^{-\alpha_k \Delta t_k}$ for exponential linearization:

$$e^{-\alpha_k \Delta t_k} \approx \frac{1 - \alpha_k \Delta t_k / 2}{1 + \alpha_k \Delta t_k / 2}.$$
 (5)

By substituting Eq.5 into Eq.4, we obtain a simplified closed-form solution:

$$\tilde{\boldsymbol{g}}(t_{k+1}) \approx (\boldsymbol{g}(t_k) - p_r) \left(\frac{1 - (\alpha_k \Delta t_k)/2}{1 + (\alpha_k \Delta t_k)/2} \right) \cdot \beta_k + p_r. \tag{6}$$

Subsequently, CFCTM updates the state g(t) of LTC neurons at each sub-intervals. For example, in k-th time interval $[t_k, t_{k+1}]$, the time-continuous reset gate r_k and update gate u_k are computed via the k-th neuronal input features P_k and the current state $g(t_k)$ Hasani et al. (2022); Chahine et al. (2023). By applying Euler integration to Eq.2, we obtain information from the preceding k-1 temporal intervals and subsequently regulate the intermediate state $\tilde{g}(t_k)$ within the k-th interval via r_k . This mechanism enables r_k to selectively attenuate the information propagated from $g(t_k)$ and previous temporal intervals. These operations can be formulated as in:

$$\tilde{\boldsymbol{g}}(t_k) = (1 - \boldsymbol{r}_k) \cdot \boldsymbol{g}(t_k) + \boldsymbol{r}_k \cdot \sum_{n=1}^{k-1} \frac{d\boldsymbol{g}(t_n)}{dt} \frac{\Delta t_n}{k}.$$
 (7)

Next, to dynamically adapt the neuron's state transition based on the characteristics of the input visual features P_k at each time step, the (k+1)-th state of LTC neurons $g(t_{k+1})$ can be calculated via $\tilde{g}(t_{k+1})$, $\tilde{g}(t_k)$, and u_k :

$$\mathbf{g}(t_{k+1}) = (1 - \mathbf{u}_k) \cdot \tilde{\mathbf{g}}(t_k) + \mathbf{u}_k \cdot \tilde{\mathbf{g}}(t_{k+1}). \tag{8}$$

Finally, through the iterative application of Eq.8 across all time intervals, the CFCTM processes $P_{\rm w}$ along with the corresponding time parameters and generates the dynamically modeled state features $G \in \mathbb{R}^{YB \times T^2 \times L}$:

$$G = CFCTM(P_{w}, MLP(M)), \tag{9}$$

where $MLP(\cdot)$ indicates the multi-layer perceptron.

3.2.3 LIQUID SELF-ATTENTION

We then perform a series of dimensional transformations and information fusion on $G \in \mathbb{R}^{NB \times T^2 \times L}$ obtained from CFCTM, including: (1) Adjust the channel number of G to 3L through a layer normalization operation. (2) Split the G into three groups of matrices along the channel dimension, including query Q, key K and value V through the splitting operation, where $Q = \{Q_1, \dots, Q_h\}, K = \{K_1, \dots, K_h\}, V = \{V_1, \dots, V_h\} \in \mathbb{R}^{NB \times T^2 \times L}$. These operations are formally defined as in:

$$Q, K, V = SP(LN(G)), \qquad (10)$$

where $SP(\cdot)$ and $LN(\cdot)$ indicate the splitting operation and layer normalization, respectively.

With these matrices, we perform the LSA operation following standard Transformer-based attention mechanisms Dosovitskiy et al. (2021); Liu et al. (2021), written by:

$$LSA(Q, K, V) = SoftMax \left(\frac{QK^{T}}{\sqrt{L}} + M\right)V.$$
(11)

The LSA output is combined with the original patch embeddings through a residual connection, followed by another MLP and normalization layer to produce the final output of the LTCFormer block:

$$\widetilde{P} = LSA(Q, K, V) + P_{Ed},$$
(12)

$$P_{o} = MLP(LN(\widetilde{P})) + \widetilde{P}.$$
(13)

3.3 LIQUID IMAGE QUALITY-AWARE FRAMEWORK

We subsequently adapt the LTCFormer for BIQA tasks by employing the LTCFormer framework for hierarchical feature extraction and a Multi-Scale Image Quality-Aware Decoder (MIQAD) for quality prediction. As illustrated in Figure 2, the patch tokens are processed through four LTCFormer stages, denoted as S_1 , S_2 , S_3 , and S_4 . The framework yields feature maps $F_i \in \mathbb{R}^{B \times (H/2^{i+1}) \times (W/2^{i+1}) \times C_i}$ at the i-th stage, where $C_i = 2^{i-1} \times C_1$ is the feature dimension at the i-th stage. The extracted feature maps F_1 , F_2 , F_3 , and F_4 from these four stages are then fed into MIQAD, which characterizes image quality from multi-perspectives.

Within MIQAD, we implement a multi-scale quality regression approach to effectively leverage the hierarchical features extracted by the LTCFormer framework. This mechanism is inspired by the multi-faceted nature of human visual perception, where quality assessment occurs simultaneously across different perceptual dimensions. In human visual evaluation, observers naturally assess images at multiple scales from fine-grained details to overall compositional harmony, and different observers often prioritizing different aspects of visual quality. MIQAD's multi-component quality assessment structure methodically reproduces this cognitive process, as shown in Figure 2, each feature map F_i , $i \in \{1, 2, 3, 4\}$ undergoes a dedicated quality regression pathway to generate scale-specific quality scores S_i . Specifically, each feature map F_i is processed through a scale-specific quality regression module consisting of global average pooling followed by a MLP. This process can be formulated as:

$$S_i = \text{MLP}_i(\text{GAP}(F_i)), \quad i \in \{1, 2, 3, 4\},$$
 (14)

where GAP represents global average pooling operation and MLP_i denotes the quality regression network for the *i*-th scale. With the score from coarse to fine, MIQAD can achieve a comprehensive evaluation of the image quality, thus reducing the prediction uncertainty. The final image quality score S is obtained by averaging these four scale-specific quality scores from Eq.14:

$$S = \frac{1}{4} \sum_{i=1}^{4} S_i. \tag{15}$$

Table 1: Quantitative comparison based on average SRCC and PLCC. Bold values denote the best result per dataset. We have detailed the trainable parameter values of mainstream SOTA models.

Method	Train Param.	LIVE	CSIQ	TID2013	LIVEC	KonIQ	LIVEFB
		PLCCSRCC	PLCCSRCC	PLCCSRCC	PLCCSRCC	PLCCSRCC	PLCCSRCC
BRISQUE	-				0.629 0.629		
ILNIQE	-	0.906 0.902	0.865 0.822	0.648 0.521	0.508 0.508	0.537 0.523	0.332 0.294
BIECON	-	0.961 0.958	0.823 0.815	0.762 0.717	0.613 0.613	0.654 0.651	0.428 0.407
MEON	-	0.955 0.951	0.864 0.852	0.824 0.808	0.710 0.697	0.628 0.611	0.394 0.365
DBCNN	-	0.971 0.968	0.959 0.946	0.865 0.816	0.869 0.851	0.884 0.875	0.551 0.545
MetaIQA	-	0.959 0.960	0.908 0.899	0.868 0.856	0.802 0.835	0.856 0.887	0.507 0.54
P2P-BM	-	0.958 0.959	0.902 0.899	0.856 0.862	0.842 0.844	0.885 0.872	0.598 0.526
HyperIQA	27M	0.966 0.962	0.942 0.923	0.858 0.840	0.882 0.859	0.917 0.906	0.602 0.544
MUSIQ	27M	0.911 0.940	0.893 0.871	0.815 0.773	0.828 0.785	0.928 0.916	0.661 0.566
TReS	152M	0.968 0.969	0.942 0.922	0.883 0.863	0.882 0.859	0.928 0.915	0.625 0.554
CLIP-IQA+	-				0.832 0.805	0.909 0.895	0.593 0.575
Q-Align	8.2B		0.936 0.915		0.921 0.931	0.934 0.935	
Re-IQA	48M	0.971 0.970	0.96 0.947	0.861 0.804	0.854 0.840	0.923 0.914	
DEIQT	24M	0.982 0.980	0.963 0.946	0.908 0.892	0.894 0.875	0.934 0.921	0.663 0.571
QFM-IQM	24M	0.983 0.981	0.965 0.954		0.913 0.891	0.936 0.922	0.667 0.567
LoDa	9M	0.979 0.975		0.901 0.869	0.899 0.876	0.944 0.932	0.679 0.578
Align-IQA	35M	0.987 0.985	0.981 0.975	0.960 0.955	0.916 0.905	0.932 0.923	
LQMamba-B	94M	0.959 0.951	0.915 0.889	0.965 0.964	0.913 0.888	0.947 0.933	0.675 0.582
LIQT (Ours)) 7M	0.988 0.985	0.983 0.976	0.964 0.958	0.925 0.919	0.939 0.926	0.682 0.586

3.4 Loss Function

We optimize our architecture by minimize the L_1 loss for BIQA, which can be formulated as:

$$\mathcal{L} = \left\| s_p - s_{gt} \right\|_1,\tag{16}$$

where $\|\cdot\|_1$ denotes the L_1 norm, s_p denotes the predicted quality score, and s_{gt} represents the corresponding ground truth score.

4 EXPERIMENTS

4.1 EXPERIMENTAL SETTINGS

Implementation Details. For LIQT training, we followed the typical training strategy outlined in DEIQT Qin et al. (2023) to randomly standardize an input image with a pixel resolution of 224×224 . Our model uses LTCFormer with MIQAD decoder to obtain MOS scores. Training runs for 9 epochs with 2×10^{-4} learning rate, applying tenfold decay every 3 epochs. Batch size varies with dataset size. For each dataset, 80% images were used for training and the remaining 20% images were utilized for testing. We repeated this process 10 times to mitigate the performance bias and the medians of SRCC and PLCC were reported, following Qin et al. (2023). All experiments run on four NVIDIA 4090 GPUs.

Compared Methods. We compared 18 popular or state-of-the-art (SOTA) methods, including CNN-based approaches such as BRISQUE Mittal et al. (2012), ILNIQE Zhang et al. (2015), BIECON Kim & Lee (2016), DBCNN Zhang et al. (2018), MetaIQA Zhu et al. (2020), P2P-BM Ying et al. (2020), HyperIQA Su et al. (2020), and Re-IQA Saha et al. (2023). Our comparison also covers Transformer-based methods like MUSIQ Ke et al. (2021), TReS Golestaneh et al. (2022), DEIQT Qin et al. (2023), and QFM-IQM Li et al. (2025), as well as CLIP-based methods such as CLIP-IQA+. Additionally, we evaluated hybrid CNN and ViT approaches including TReS Golestaneh et al. (2022), LoDa Xu et al. (2024), Align-IQA Yang et al. (2024) along with the LLM-based Q-Align Wu et al. (2023), and LQMamba-B Guan et al. (2025). We report detailed SRCC and PLCC performance across multiple datasets, with results sourced either from original papers or reproduced using publicly available code.

Benchmark Datasets. We evaluated the LIQT on six public Image Quality Assessment (IQA) datasets. Among these, LIVEC Ghadiyaram & Bovik (2016) and KonIQ-10k Hosu et al. (2020)

contain authentic distortions, while LIVE Sheikh et al. (2006), CSIQ Chandler (2010), TID2013 Ponomarenko et al. (2015), and LIVEFB Ying et al. (2020) feature synthetic distortions. The LIVEC dataset comprises 1,162 images with diverse real-world distortions, whereas KonIQ-10k includes 10,073 images sourced from open multimedia repositories. LIVEFB represents the largest real distortion dataset, containing 39,810 images. Synthetic datasets typically contain a limited number of pristine images with applied artificial distortions such as Gaussian blur and JPEG compression. The LIVE and CSIQ datasets include 779 and 866 synthetic images, respectively, covering 5 and 6 distortion categories. TID2013 offers more extensive collections, with 3,000 images exhibiting 24 distortion types.

Evaluation Metrics. For evaluation metrics, we employed the Spearman Rank Correlation Coefficient (SRCC) and Pearson Linear Correlation Coefficient (PLCC) to assess monotonicity and accuracy, with values ranging from -1 to 1, where coefficients approaching 1 indicate superior predictive performance.

4.2 QUANTITATIVE AND QUALITATIVE COMPARISON

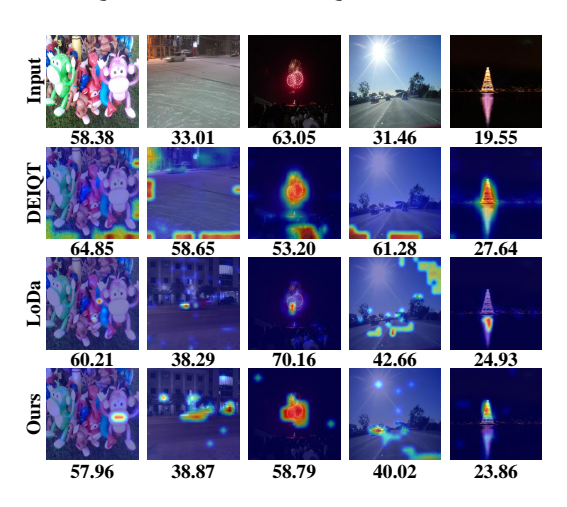


Figure 3: Activation maps of DEIQT, LoDa, and LIQT, drawn using the Grad-CAM method Selvaraju et al. (2017). The figure also shows the MOS. Our LIQT model is designed to focus more on spatiotemporal feature aggregation of images, thereby improving image quality prediction performance. Rows 1-4 in the figure represent the input images, DEIQT, LoDa, and LIQT's CAMs, respectively.

In Section 4.1, we reported on competing models and their corresponding backbones, presenting detailed comparison results in Table 1. LIQT achieved highly competitive performance among existing models. Since these datasets cover a wide range of distortion types and image content, achieving competitive performance across them is challenging. Notably, we achieved the best results on the most challenging LIVEFB dataset, as the prevalent local distortions in LIVEFB align with the spatiotemporal aggregation characteristics of liquid neural networks. Meanwhile, it should be emphasized that we only used 7M trainable parameters, as sequential tasks inherently possess memory capabilities and do not require excessive training parameters. This better matches the characteristics of image quality assessment, that estimators can remember most image features without needing multiple comparisons during eval-

In addition to the quantitative comparison, we present qualitative comparison results in Figure 3 to depict the visual results of the activation maps from DEIQT, LoDa, and LIQT. DEIQT's activation maps primarily focus on

high-contrast regions and object boundaries, LoDa shows improved attention distribution. LIQT's activation maps demonstrate more comprehensive coverage of perceptually important regions, attending to both structural elements and texture details. This enhanced spatiotemporal feature aggregation aligns better with human visual perception, as confirmed by the Mean Opinion Scores (MOS).

4.3 Cross-Dataset Evaluation

To further evaluate the generalization ability of LIQT, we conducted cross-dataset validation. Specifically, our model was trained on one dataset and then tested on another dataset without any fine-tuning or parameter adaptation. To ensure simplicity and universality, we conducted several sets of experiments. The experimental results are represented by the average SRCC values on these datasets. Encouragingly, LIQT achieved state-of-the-art performance in all experiments, despite having fewer trainable parameters than the compared methods. Through spatiotemporal aggregation of streaming neural networks, our model can better understand key quality representation spaces

Table 2: SRCC on the cross datasets validation. The best performances are highlighted in boldface.

Training	LIV	EFB	LIVEC	KonIQ	LIVE	CSIQ
Testing	KonIQ	LIVEC	KonIQ	LIVEC	CSIQ	LIVE
DBCNN	0.716	0.724	0.754	0.755	0.758	0.877
P2P-BM	0.755	0.738	0.740	0.770	0.712	-
TReS	0.713	0.740	0.733	0.786	0.761	-
DEIQT	0.733	0.781	0.744	0.794	0.781	0.932
LoDa	0.763	0.805	0.745	0.811	-	-
LIQT (Ours)	0.771	0.810	0.741	0.807	0.792	0.937

Table 3: Ablation study on LIVEC and KonIQ datasets. Each row shows the performance with different combinations of components: α_k , β_k , CFCTM, LSA, and MIQAD. The best performances are highlighted in boldface.

LIVEC

α_k	β_k	CFCTM	LSA	MIQAD	LIVEC		KoniQ	
					PLCC	SRCC	PLCC	SRCC
					0.818	0.806	0.842	0.833
				\checkmark	0.832	0.824	0.857	0.849
\checkmark			\checkmark	\checkmark	0.853	0.849	0.872	0.869
	\checkmark		\checkmark	\checkmark	0.844	0.835	0.863	0.856
		\checkmark	\checkmark	\checkmark	0.867	0.854	0.877	0.868
\checkmark	\checkmark		\checkmark	\checkmark	0.876	0.870	0.881	0.874
\checkmark		\checkmark	\checkmark	\checkmark	0.903	0.894	0.922	0.913
	\checkmark	\checkmark	\checkmark	\checkmark	0.899	0.887	0.905	0.896
\checkmark	\checkmark	\checkmark		\checkmark	0.880	0.874	0.885	0.878
\checkmark	√	√	✓	√	0.925	0.919	0.939	0.926

rather than the decoupled collapse of existing neural networks, thus achieving robust generalization ability with a streaming structure.

4.4 ABLATION STUDY

Table 3 presents a comprehensive ablation analysis of LIQT's key components on LIVEC and KonIQ datasets, examining individual and combined contributions of decay rate α_k , modulation factor β_k , CFCTM, LSA, and MIQAD modules. The first row represents a pure Swin Transformer baseline without any of our proposed components. The results demonstrate the progressive contribution of each component to the overall performance. The pure Swin Transformer baseline serves as our reference point, with MIQAD alone providing improvements, demonstrating the effectiveness of multi-scale quality assessment. CFCTM provides the most significant individual contribution among liquid neural components, and removing LSA while maintaining other components substantially reduces performance, highlighting the critical role of LSA.

5 Conclusion

In this paper, we introduced LIQT, a novel BIQA framework that addresses the STRD challenge by integrating biomimetic neural mechanisms. We developed CFCTM that reformulates liquid neuronal dynamics into stable closed-form solutions, enabling continuous-time processing aligned with human visual perception. LTCFormer dynamically modulates feature extraction based on local image features through LSA mechanism. MIQAD effectively emulates the multi-faceted nature of human visual assessment through scale-specific quality regression pathways. Experimental results on six benchmark datasets spanning various distortion types and image content demonstrate that LIQT consistently outperforms state-of-the-art BIQA methods.

ETHICS STATEMENT

This work adheres to the ICLR Code of Ethics. In this study, no human subjects or animal experimentation was involved. All datasets used were sourced in compliance with relevant usage guidelines, ensuring no violation of privacy. We have taken care to avoid any biases or discriminatory outcomes in our research process. No personally identifiable information was used, and no experiments were conducted that could raise privacy or security concerns. We are committed to maintaining transparency and integrity throughout the research process.

REPRODUCIBILITY STATEMENT

To ensure the reproducibility of our research, the source code for the proposed LIQT model, along with training and evaluation scripts, is provided in the Supplementary Material. The implementation details, hyper-parameters, and experimental setup described in Section 4.1 of the main paper are sufficient to replicate the reported results. Additionally, the six IQA benchmark datasets are publicly available, ensuring consistent and reproducible evaluation results. We believe these measures will enable other researchers to reproduce our work and further advance the field.

REFERENCES

- Omran Ayoub, Davide Andreoletti, Aleksandra Knapińska, Róża Goścień, Piotr Lechowicz, Tiziano Leidi, Silvia Giordano, Cristina Rottondi, and Krzysztof Walkowiak. Liquid neural networkbased adaptive learning vs. incremental learning for link load prediction amid concept drift due to network failures. *arXiv preprint arXiv:2404.05304*, 2024.
- Makram Chahine, Ramin Hasani, Patrick Kao, Aaron Ray, Ryan Shubert, Mathias Lechner, Alexander Amini, and Daniela Rus. Robust flight navigation out of distribution with liquid neural networks. *Science Robotics*, 8(77):eadc8892, 2023.
- Larson Damon M. Chandler. Most apparent distortion: full-reference image quality assessment and the role of strategy. *Journal of Electronic Imaging*, 19(1):011006, 2010.
- Chaofeng Chen, Jiadi Mo, Jingwen Hou, Haoning Wu, Liang Liao, Wenxiu Sun, Qiong Yan, and Weisi Lin. Topiq: A top-down approach from semantics to distortions for image quality assessment. *IEEE Transactions on Image Processing*, 2024.
- Hanting Chen, Yunhe Wang, Tianyu Guo, Chang Xu, Yiping Deng, Zhenhua Liu, Siwei Ma, Chunjing Xu, Chao Xu, and Wen Gao. Pre-trained image processing transformer. In *International Conference on Computer Vision and Pattern Recognition (CVPR)*, 2021.
- Alexey Dosovitskiy, Lucas Beyer, Alexander Kolesnikov, Dirk Weissenborn, Xiaohua Zhai, Thomas Unterthiner, Mostafa Dehghani, Matthias Minderer, Georg Heigold, Sylvain Gelly, Jakob Uszkoreit, and Neil Houlsby. An image is worth 16x16 words: Transformers for image recognition at scale. *ICLR*, 2021.
- Deepti Ghadiyaram and Alan C. Bovik. Massive online crowdsourced study of subjective and objective picture quality. *IEEE Transactions on Image Processing*, 25(1):372–387, 2016.
- S Alireza Golestaneh, Saba Dadsetan, and Kris M Kitani. No-reference image quality assessment via transformers, relative ranking, and self-consistency. In *Proceedings of the IEEE/CVF Winter Conference on Applications of Computer Vision*, pp. 1220–1230, 2022.
- Fengbin Guan, Xin Li, Zihao Yu, Yiting Lu, and Zhibo Chen. Qmamba: On first exploration of vision mamba for image quality assessment. In *Proceedings of the 42nd International Conference on Machine Learning*, ICML'25, 2025.
- Ramin Hasani, Mathias Lechner, Alexander Amini, Daniela Rus, and Radu Grosu. Liquid time-constant networks. In *AAAI Conference on Artificial Intelligence*, 2020.
- Ramin Hasani, Mathias Lechner, Alexander Amini, Lucas Liebenwein, Aaron Ray, Max Tschaikowski, Gerald Teschl, and Daniela Rus. Closed-form continuous-time neural networks. *Nature Machine Intelligence*, November 2022. ISSN 2522-5839.

- Vlad Hosu, Hanhe Lin, Tamas Sziranyi, and Dietmar Saupe. Koniq-10k: An ecologically valid database for deep learning of blind image quality assessment. *IEEE Transactions on Image Processing*, 29:4041–4056, 2020.
 - Prakash Kumar Karn, Iman Ardekani, and Waleed H. Abdulla. Generalized framework for liquid neural network upon sequential and non-sequential tasks. *Mathematics*, 12(16), 2024. ISSN 2227-7390.
 - Junjie Ke, Qifei Wang, Yilin Wang, Peyman Milanfar, and Feng Yang. Musiq: Multi-scale image quality transformer. In *Proceedings of the IEEE/CVF International Conference on Computer Vision*, pp. 5148–5157, 2021.
 - Jongyoo Kim and Sanghoon Lee. Fully deep blind image quality predictor. *IEEE Journal of selected topics in signal processing*, 11(1):206–220, 2016.
 - Mathias Lechner, Ramin Hasani, Alexander Amini, Thomas A Henzinger, Daniela Rus, and Radu Grosu. Neural circuit policies enabling auditable autonomy. *Nature Machine Intelligence*, 2(10): 642–652, 2020.
 - Xudong Li, Timin Gao, Runze Hu, Yan Zhang, Shengchuan Zhang, Xiawu Zheng, Jingyuan Zheng, Yunhang Shen, Ke Li, Yutao Liu, Pingyang Dai, and Rongrong Ji. Adaptive feature selection for no-reference image quality assessment by mitigating semantic noise sensitivity. In *Proceedings of the 41st International Conference on Machine Learning*, ICML'24. JMLR.org, 2025.
 - Ze Liu, Yutong Lin, Yue Cao, Han Hu, Yixuan Wei, Zheng Zhang, Stephen Lin, and Baining Guo. Swin transformer: Hierarchical vision transformer using shifted windows. In *Proceedings of the IEEE/CVF International Conference on Computer Vision (ICCV)*, 2021.
 - Ze Liu, Han Hu, Yutong Lin, Zhuliang Yao, Zhenda Xie, Yixuan Wei, Jia Ning, Yue Cao, Zheng Zhang, Li Dong, Furu Wei, and Baining Guo. Swin transformer v2: Scaling up capacity and resolution. In *International Conference on Computer Vision and Pattern Recognition (CVPR)*, 2022.
 - Anish Mittal, Anush Krishna Moorthy, and Alan Conrad Bovik. No-reference image quality assessment in the spatial domain. *IEEE Transactions on image processing*, 21(12):4695–4708, 2012.
 - Anush Krishna Moorthy and Alan Conrad Bovik. Blind image quality assessment: From natural scene statistics to perceptual quality. *IEEE Transactions on Image Processing*, 20(12):3350–3364, 2011.
 - Nikolay Ponomarenko, Lina Jin, Oleg Ieremeiev, Vladimir Lukin, Karen Egiazarian, Jaakko Astola, Benoit Vozel, Kacem Chehdi, Marco Carli, Federica Battisti, and C.-C. Jay Kuo. Image database tid2013: Peculiarities, results and perspectives. *Signal Processing: Image Communication*, 30: 57–77, 2015. ISSN 0923-5965.
 - Guanyi Qin, Runze Hu, Yutao Liu, Xiawu Zheng, Haotian Liu, Xiu Li, and Yan Zhang. Data-efficient image quality assessment with attention-panel decoder. In *AAAI Conference on Artificial Intelligence*, pp. 2091–2100, 2023.
 - Avinab Saha, Sandeep Mishra, and Alan C Bovik. Re-iqa: Unsupervised learning for image quality assessment in the wild. In *Proceedings of the IEEE/CVF Conference on Computer Vision and Pattern Recognition*, pp. 5846–5855, 2023.
 - Ramprasaath R Selvaraju, Michael Cogswell, Abhishek Das, Ramakrishna Vedantam, Devi Parikh, and Dhruv Batra. Grad-cam: Visual explanations from deep networks via gradient-based localization. In *Proceedings of the IEEE international conference on computer vision*, pp. 618–626, 2017.
 - H.R. Sheikh, M.F. Sabir, and A.C. Bovik. A statistical evaluation of recent full reference image quality assessment algorithms. *IEEE Transactions on Image Processing*, 15(11):3440–3451, 2006.
 - Shaolin Su, Qingsen Yan, Yu Zhu, Cheng Zhang, Xin Ge, Jinqiu Sun, and Yanning Zhang. Blindly assess image quality in the wild guided by a self-adaptive hyper network. In *Proceedings of the IEEE/CVF Conference on Computer Vision and Pattern Recognition*, pp. 3667–3676, 2020.

- C.J. van den Branden Lambrecht. A working spatio-temporal model of the human visual system for image restoration and quality assessment applications. In 1996 IEEE International Conference on Acoustics, Speech, and Signal Processing Conference Proceedings, volume 4, pp. 2291–2294 vol. 4, 1996.
 - Zhou Wang, A.C. Bovik, H.R. Sheikh, and E.P. Simoncelli. Image quality assessment: from error visibility to structural similarity. *IEEE Transactions on Image Processing*, 13(4):600–612, 2004.
 - Haoning Wu, Zicheng Zhang, Weixia Zhang, Chaofeng Chen, Chunyi Li, Liang Liao, Annan Wang, Erli Zhang, Wenxiu Sun, Qiong Yan, Xiongkuo Min, Guangtai Zhai, and Weisi Lin. Q-align: Teaching lmms for visual scoring via discrete text-defined levels. *arXiv preprint arXiv:2312.17090*, 2023. Equal Contribution by Wu, Haoning and Zhang, Zicheng. Project Lead by Wu, Haoning. Corresponding Authors: Zhai, Guangtai and Lin, Weisi.
 - Kangmin Xu, Liang Liao, Jing Xiao, Chaofeng Chen, Haoning Wu, Qiong Yan, and Weisi Lin. Boosting image quality assessment through efficient transformer adaptation with local feature enhancement. In *Proceedings of the IEEE/CVF Conference on Computer Vision and Pattern Recognition*, pp. 2662–2672, 2024.
 - Jiebin Yan, Yuming Fang, Liping Huang, Xiongkuo Min, Yiru Yao, and Guangtao Zhai. Blind stereoscopic image quality assessment by deep neural network of multi-level feature fusion. In 2020 IEEE International Conference on Multimedia and Expo (ICME), pp. 1–6, 2020. doi: 10. 1109/ICME46284.2020.9102888.
 - Junfeng Yang, Jing Fu, Zhen Zhang, Limei Liu, Qin Li, Wei Zhang, and Wenzhi Cao. Aligniqa: aligning image quality assessment models with diverse human preferences via customizable guidance. In *Proceedings of the 32nd ACM International Conference on Multimedia*, pp. 10008–10017, 2024.
 - Xiaohan Yang, Fan Li, and Hantao Liu. A survey of dnn methods for blind image quality assessment. *IEEE Access*, 7:123788–123806, 2019.
 - Zhenqiang Ying, Haoran Niu, Praful Gupta, Dhruv Mahajan, Deepti Ghadiyaram, and Alan Bovik. From patches to pictures (paq-2-piq): Mapping the perceptual space of picture quality. In *Proceedings of the IEEE/CVF Conference on Computer Vision and Pattern Recognition*, pp. 3575–3585, 2020.
 - Lin Zhang, Lei Zhang, and Alan C Bovik. A feature-enriched completely blind image quality evaluator. *IEEE Transactions on Image Processing*, 24(8):2579–2591, 2015.
 - Weixia Zhang, Kede Ma, Jia Yan, Dexiang Deng, and Zhou Wang. Blind image quality assessment using a deep bilinear convolutional neural network. *IEEE Transactions on Circuits and Systems for Video Technology*, 30(1):36–47, 2018.
 - Weixia Zhang, Guangtao Zhai, Ying Wei, Xiaokang Yang, and Kede Ma. Blind image quality assessment via vision-language correspondence: A multitask learning perspective. In *Proceedings of the IEEE/CVF Conference on Computer Vision and Pattern Recognition*, pp. 14071–14081, 2023.
 - Kai Zhao, Kun Yuan, Ming Sun, Mading Li, and Xing Wen. Quality-aware pre-trained models for blind image quality assessment. In *Proceedings of the IEEE/CVF Conference on Computer Vision and Pattern Recognition*, pp. 22302–22313, 2023.
 - Hancheng Zhu, Leida Li, Jinjian Wu, Weisheng Dong, and Guangming Shi. Metaiqa: Deep metalearning for no-reference image quality assessment. In *Proceedings of the IEEE/CVF Conference* on Computer Vision and Pattern Recognition, pp. 14143–14152, 2020.

A APPENDIX

A.1 THE USE OF LARGE LANGUAGE MODELS (LLMS)

Large Language Models (LLMs) were used to aid in the writing and polishing of the manuscript. Specifically, we used an LLM to assist in refining the language, improving readability, and ensuring clarity in various sections of the paper. The model helped with tasks such as sentence rephrasing, grammar checking, and enhancing the overall flow of the text.

It is important to note that the LLM was not involved in the ideation, research methodology, or experimental design. All research concepts, ideas, and analyses were developed and conducted by the authors. The contributions of the LLM were solely focused on improving the linguistic quality of the paper, with no involvement in the scientific content or data analysis.

The authors take full responsibility for the content of the manuscript, including any text generated or polished by the LLM. We have ensured that the LLM-generated text adheres to ethical guidelines and does not contribute to plagiarism or scientific misconduct.

A.2 DERIVATION OF CLOSED-FORM SOLUTIONS FOR LIQUID TIME-CONSTANT NEURONS

The fundamental dynamics of LTC neurons are governed by the differential equation presented in Eq.1 Hasani et al. (2022). To derive the closed-form solution that enables efficient computation, we begin with the differential equation governing the membrane potential q(t) of an LTC neuron:

$$\frac{d\boldsymbol{g}\left(t\right)}{dt} = -\left[\boldsymbol{l} + f\left(\boldsymbol{P}\left(t\right)\right)\right] \cdot \boldsymbol{g}\left(t\right) + f\left(\boldsymbol{P}\left(t\right)\right) \cdot p_{r},\tag{17}$$

where l is the leakage conductance vector of the LTC neurons Lechner et al. (2020), f(P(t)) is a nonlinear function of the exogenous input signal P(t), and p_r is the reversal potential of LTC neurons. For computational tractability, we assume that over a small time interval $[t_k, t_{k+1}]$, the input signal P(t) is piecewise constant Lechner et al. (2020). This allows us to define two learnable, input-dependent parameters for that interval:

- The decay rate: $\alpha_k = \boldsymbol{l} + f(\boldsymbol{P}_k)$.
- The modulation factor: $\beta_k = f(\mathbf{P}_k)$.

Substituting these into Eq.17 yields a simplified linear ordinary differential equation (ODE):

$$\frac{d\mathbf{g}(t)}{dt} = -\alpha_k \cdot \mathbf{g}(t) + \beta_k \cdot p_r. \tag{18}$$

To solve this, we first rearrange it into the standard form for a first-order linear ODE:

$$\frac{d\boldsymbol{g}(t)}{dt} + \alpha_k \boldsymbol{g}(t) = \beta_k p_r. \tag{19}$$

The general solution is the sum of the homogeneous solution $g_h(t)$ and a particular solution $g_p(t)$. The homogeneous part of the equation is:

$$\frac{d\mathbf{g}_h}{dt} + \alpha_k \mathbf{g}_h = 0. {20}$$

The solution to this separable equation is $g_h(t) = Ce^{-\alpha_k t}$, where C is the constant of integration. For the particular solution, since the right-hand side of Eq.19 is a constant, we assume a constant particular solution $g_p(t) = Z$. Substituting this into Eq.19 gives:

$$\frac{dZ}{dt} + \alpha_k Z = \beta_k p_r. \tag{21}$$

Since Z is a constant, its derivative is zero, which simplifies to $\alpha_k Z = \beta_k p_r$, so $Z = \frac{\beta_k p_r}{\alpha_k}$. Therefore, the general solution is:

$$\mathbf{g}(t) = \mathbf{g}_h(t) + \mathbf{g}_p(t) = Ce^{-\alpha_k t} + \frac{\beta_k p_r}{\alpha_k}.$$
 (22)

We determine the integration constant C using the initial condition at the start of the interval, t = 0, where the membrane potential is $g(0) = g_0$. Substituting this into the general solution gives:

$$g_0 = Ce^0 + \frac{\beta_k p_r}{\alpha_k} \implies C = g_0 - \frac{\beta_k p_r}{\alpha_k}.$$
 (23)

Substituting this expression for C back into the general solution (Eq.22) yields the exact solution for the interval:

$$\mathbf{g}(t) = \left(\mathbf{g}_0 - \frac{\beta_k p_r}{\alpha_k}\right) e^{-\alpha_k t} + \frac{\beta_k p_r}{\alpha_k}.$$
 (24)

This solution can be rearranged by expanding the terms and factoring out g_0 and $\frac{\beta_k p_r}{\alpha_k}$:

$$\mathbf{g}(t) = \mathbf{g}_0 e^{-\alpha_k t} + \frac{\beta_k p_r}{\alpha_k} (1 - e^{-\alpha_k t}). \tag{25}$$

While Eq. 25 represents the exact solution, the term $(\beta_k p_r)/\alpha_k$ can introduce numerical instability if $\alpha_k = l + f(P_k)$ becomes close to zero during training. This can happen if the leakage l is small and the input activation $f(P_k)$ is also close to zero, leading to potential division-by-zero errors and training instability. To ensure a robust implementation, we adopt an alternative, more numerically stable formulation inspired by prior work Lechner et al. (2020); Hasani et al. (2022); Karn et al. (2024). This formulation approximates the steady-state value $\frac{\beta_k p_r}{\alpha_k}$ with an interpolation controlled by β_k , leading to the following equivalent but more stable parameterization:

$$\mathbf{g}(t) \approx (\mathbf{g}_0 - p_r) e^{-\alpha_k t} \cdot \beta_k + p_r. \tag{26}$$

This form represents the state at time t as an interpolation between the initial state g_0 and the reversal potential p_r , driven by input-dependent dynamics. It avoids explicit division by α_k , replacing it with multiplications that are numerically more robust. This closed-form solution allows us to bypass computationally expensive numerical integration methods like Runge-Kutta, while preserving the core dynamics of the continuous-time system Hasani et al. (2022); Karn et al. (2024).

A.3 ANALYSIS OF THE PADÉ APPROXIMANT IN CFCTM

In our Closed-Form Continuous-Time Module (CFCTM), we approximate the exponential term $e^{-\alpha_k \Delta t_k}$ using the (1,1)-order Padé approximant, as shown in Eq. 5. The approximant is given by:

$$e^{-x} \approx \frac{1 - x/2}{1 + x/2}. (27)$$

We select this method over alternatives such as the first-order Taylor series expansion ($e^{-x} \approx 1 - x$) based on the following considerations.

Regarding numerical stability, the Taylor expansion becomes negative when x>1, which may lead to unstable liquid neural dynamics when the decay term $\alpha_k \Delta t_k$ is large. The Padé approximant remains positive for all $x\geq 0$ and asymptotically approaches -1 as $x\to\infty$. Its value is therefore bounded, which helps prevent unstable state dynamics during training.

In terms of approximation accuracy, the Padé approximant matches the Taylor series of e^{-x} up to the second order, providing higher approximation accuracy over a wider range of x values compared to the first-order Taylor expansion. This allows the discretized dynamics of our model to more closely approximate the underlying continuous-time system.

From a computational efficiency perspective, this approximation requires only basic arithmetic operations (division, addition, and subtraction), which are already optimized on modern hardware such as GPUs. This enables our CFCTM to avoid the computational overhead of repeatedly calculating the exponential function during each forward pass.